

A 3D Forward and Back-Projection Method for X-Ray CT Using Separable Footprint

Yong Long, Jeffrey A. Fessler and James M. Balter

Abstract—The computation burden of cone-beam forward and back-projectors is one of the greatest challenges facing iterative methods for 3D image reconstruction in CT. This paper describes a new separable footprint (SF) projector. It takes advantage of small polar angles of X-rays in cone-beam geometry to approximate the voxel footprint functions as 2D separable functions with simple rectangular functions in the axial direction. Due to rotation of the source, a more accurate function is adopted to approximate the footprint function in the transaxial direction, such as a trapezoid function. Because of the separability of these footprint functions, calculating their integrals over a detector cell is greatly simplified and can be implemented efficiently. Simulations and experiments showed that the SF projector is more accurate with similar computational speed than the distance-driven (DD) projector, which is a current state-of-the-art method in the field.

Index Terms—Cone-beam tomography, iterative tomographic image reconstruction, forward and back-projection

I. INTRODUCTION

Iterative statistical methods for 3D tomographic image reconstruction offer numerous advantages such as the potential for improved image quality and reduced dose, as compared to the conventional methods such as filtered back-projection (FBP). The primary computational bottleneck in iterative reconstruction methods is forward and back-projections. The forward projection is roughly a discretized evaluation of the Radon transform, and the back-projector is the adjoint of the forward projector. Traditionally the forward and back-projection steps involve operations such as computing the lengths of intersections between each tomographic ray and each image basis function.

A variety of methods for 3D forward and back-projection have been proposed [1]–[6]. All methods provide some compromise between computational complexity and accuracy.

Although spherically symmetric basis functions (blobs) have many advantages over simple cubic voxels or other basis functions for the image representation, *e.g.*, their appearance is independent of the viewing angle, evaluating integrals of their footprint functions is computationally intensive. Ziegler *et al.* [3] proposed to store the integrals of their footprint functions in a lookup-table, but the computation of forward and back-projection is still large due to loading a large table and the fact that blobs intersect many more tomographic rays than voxels.

The distance-driven (DD) projector [2] is a current state-of-the-art method. It maps the horizontal and vertical boundaries of the image voxels and detector cells onto a common plane such as xz or yz plane, approximating their shapes by rectangles, calculates the lengths of overlap along the x (or y) direction and along the z direction, and then multiplies them to get the area of overlap. The DD projector has the largest errors when azimuthal angle of the X-ray source is around multiples of $\pi/4$, because the transaxial footprint is approximately triangular rather than rectangular at those angles.

We have developed a new approach for 3D forward and back-projection that we call the separable footprint (SF) projector. It approximates the voxel footprint functions as 2D separable functions. This approximation is reasonable for typical axial or helical cone-beam CT geometries. The separability of these footprint functions greatly simplifies the calculation of their integrals over a detector cell and allows efficient implementation of the new projector. Our studies showed that the SF projector is more accurate with similar computational speed than the DD projector.

The organization of this paper is as follows. Section 2 describes the cone-beam 3D system model, and introduces the SF projector and its acceleration. Section 3 gives simulation results, including accuracy and speed comparison between the SF and DD projector as stand alone modules and within iterative image reconstruction of a region of interest (ROI) method [7]. Finally, conclusions are in Section 5.

II. METHOD

A. Cone-Beam 3D System Model

In the practice of iterative image reconstruction, rather than operating on a continuous object $f(\vec{x})$, we want to forward project a discretized object based on a common basis function $\beta_0(\vec{x})$ superimposed on a $N_1 \times N_2 \times N_3$ Cartesian grid as follows:

$$f(\vec{x}) = \sum_{\vec{n}} f[\vec{n}] \beta_0 \left(\frac{1}{\Delta} \odot (\vec{x} - \vec{x}_c[\vec{n}]) \right), \quad (1)$$

where the sum is over the $N_1 \times N_2 \times N_3$ lattice, $\vec{x}_c[\vec{n}]$ denotes the center of the \vec{n} th basis function and $\vec{n} = (n_1, n_2, n_3)$. The grid spacing is $\vec{\Delta} = (\Delta_x, \Delta_y, \Delta_z)$. We consider the case $\Delta_x = \pm \Delta_y$ hereafter, but we allow $\Delta_x \neq \Delta_z$.

Axial cone-beam projection space is characterized by three independent indices (s, t, β) , where β denotes the angle of the source point counter-clockwise from the y axis, and (s, t) denote the local coordinates on the 2D detector plane where

This work was supported in part by NIH grant P01-CA59827.

Y. Long and J. Fessler are with Dept. of Electrical Engineering and Computer Science, University of Michigan, Ann Arbor, MI 48109.

J. Balter is with Dept. of Radiation Oncology, University of Michigan, Ann Arbor, MI 48109

the s -axis is perpendicular to the z -axis and the t -axis is parallel to the z -axis.

The cone-beam projections of $f(\vec{x})$ are given by

$$p(s, t; \beta) = \int_{\mathcal{L}(s, t, \beta)} f(x, y, z) d\ell, \quad (2)$$

where

$$\mathcal{L}(s, t, \beta) = \left\{ \vec{p}_0 + \alpha \vec{e}_3 : \alpha \in [0, \sqrt{D_{sd}^2 + s^2 + t^2}] \right\},$$

\vec{e}_3 denotes the direction vector of a ray from the source position \vec{p}_0 to a point \vec{p}_1 on the detector plane, and D_{sd} denotes the source to detector distance.

Assume that the detector blur $h(s, t)$ is shift invariant, independent of β , and acts only along the s and t coordinates. Then the mean projections satisfy

$$\bar{y}_\beta[s_k, t_l] = \iint h(s_k - s, t_l - t) p(s, t; \beta) ds dt, \quad (3)$$

where (s_k, t_l) denotes the center of detector cell specified by indices (k, l) for $k = 0, \dots, N_s - 1$ and $l = 0, \dots, N_t - 1$.

Using the basis expansion model (1) for the object leads to the linear model

$$\bar{y}_\beta[s_k, t_l] = \sum_{\vec{n} \in S} a_\beta[s_k, t_l; \vec{n}] f[\vec{n}],$$

where the elements of cone-beam system matrix \mathbf{A} are samples of the following cone-beam projection of a single basis function centered at $\vec{x}_c[\vec{n}]$:

$$\begin{aligned} a_\beta[s_k, t_l; \vec{n}] &= \iint h(s_k - s, t_l - t) q(s, t; \beta; \vec{n}) ds dt \\ &= F(s_k, t_l; \beta; \vec{n}), \end{aligned} \quad (4)$$

where

$$F(s, t; \beta; \vec{n}) \triangleq \iint h(s - s', t - t') q(s', t'; \beta; \vec{n}) ds' dt',$$

which is the ‘‘blurred footprint’’ function and $q(s, t; \beta; \vec{n})$ denotes the cone-beam footprint of basis function $\beta_0 \left(\frac{1}{\Delta} \odot (\vec{x} - \vec{x}_c[\vec{n}]) \right)$. *i.e.*,

$$q(s, t; \beta; \vec{n}) = \int_{\mathcal{L}(s, t, \beta)} \beta_0 \left(\frac{1}{\Delta} \odot (\vec{x} - \vec{x}_c[\vec{n}]) \right) d\ell. \quad (5)$$

A simple model for the detector blur is

$$h(s, t) = \frac{1}{r_s r_t} \text{rect} \left(\frac{s}{r_s} \right) \text{rect} \left(\frac{t}{r_t} \right), \quad (6)$$

where r_s and r_t denote the width along s and t respectively. This model accounts for the finite size of the detector elements.

B. Separable Footprint (SF) Projector and Its Acceleration

The footprints of cubic voxel basis functions can be computed analytically for cone-beam geometries [8, p. 104]. Fig. 1 shows an example of a true footprint and its profiles.

Inspired by the shape of the true footprint, we approximate it as a 2D separable function with a rectangular function in

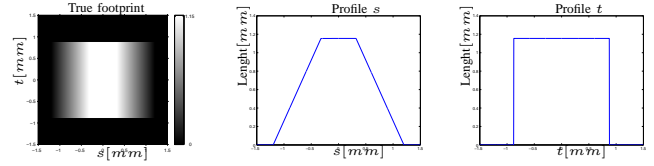


Fig. 1. An example of true footprint function and its profiles of a voxel with $\Delta_x = \Delta_y = \Delta_z = 1\text{mm}$ centered at the origin under a flat-detector cone-beam geometry with $D_{sd} = 949\text{mm}$ and $D_{s0} = 541\text{mm}$ (D_{s0} is the source to rotation center distance) when $\beta = 30^\circ$.

the axial direction and a trapezoid function in the transaxial direction as follows,

$$q(s, t; \beta; \vec{n}) \approx \Delta_x l(\beta; \vec{n}) \text{rect} \left(\frac{t - t_0}{w_{t0}} \right) \text{trap}(s; \tau_0, \tau_1, \tau_2, \tau_3), \quad (7)$$

where

$$\begin{aligned} l(\beta; \vec{n}) &\triangleq \frac{1}{|\cos(\theta_0)| \cdot \max\{|\cos(\varphi_0)|, |\sin(\varphi_0)|\}}, \\ \text{trap}(s; \tau_0, \tau_1, \tau_2, \tau_3) &\triangleq \begin{cases} \frac{s - \tau_0}{\tau_1 - \tau_0}, & \tau_0 < s < \tau_1 \\ 1, & \tau_1 \leq s \leq \tau_2 \\ \frac{\tau_3 - s}{\tau_3 - \tau_2}, & \tau_2 < s < \tau_3 \\ 0, & \text{otherwise} \end{cases} \\ t_0 &= \frac{t_l + t_r}{2}, \\ w_{t0} &= t_r - t_l, \quad t_r \geq t_l, \end{aligned} \quad (8)$$

where θ_0 and φ_0 denote the polar and azimuthal angles of the ray connecting the source and center of the \vec{n} th voxel respectively, τ_0, τ_1, τ_2 and τ_3 denote vertices of the trapezoid function which are at the exact locations as those of the true footprint function in the s direction, and t_l and t_r denote the boundaries of the rectangular function which are the projected t coordinates of two axial boundaries of the voxel. Since the boundaries of the separable function are determined by the projections of boundaries of the voxel basis function under the cone-beam geometry, the depth-dependent magnification is accurately modeled.

The scale $l(\beta; \vec{n})$ depends on angles (θ_0, φ_0) of the ray connecting the source and center of the \vec{n} th voxel. This means that $N_1 \times N_2 \times N_3 \times N_\beta$ different $l(\beta; \vec{n})$ values have to be computed, where N_β denotes the number of projection views. In addition, computing the angles for each voxel at each projection view usually involves two \tan^{-1} functions.

To accelerate the computation of the SF projector, we propose a method that initially ignores $l(\beta; \vec{n})$ by setting $l(\beta; \vec{n}) = 1$ for all the voxels at any projection view, and then scales the ‘‘blurred footprint’’ functions by multiplying them by a ray-dependent scale factor. There are many fewer tomographic rays ($n_s \times n_t$) than voxels in a 3D image ($N_1 \times N_2 \times N_3$), so this saves substantial computation.

This acceleration method utilizes the fact that for small basis functions and narrow blurs h , the angles of rays that intersect the basis function are very similar. This method is similar to Joseph’s method [9] where the scale of the triangular footprint function is determined by $1 / \max\{|\cos \varphi|, |\sin \varphi|\}$ for 2D fan-beam geometry.

The system matrix model (4) is used for both the SF forward and back projector, which ensures they are the exact adjoint operators of each other.

III. RESULT

A. Forward and Back-Projector as Single Modules

We simulated an axial cone-beam flat-detector X-ray CT system with a detector size of $N_s \times N_t = 512 \times 512$ cells spaced by $\Delta_s = \Delta_t = 1\text{mm}$ with $N_\beta = 984$ angles over 360° . The source to detector distance D_{sd} is 949mm, and the source to rotation center distance D_{s0} is 541mm. We included a rectangular detector response (6) with $r_s = \Delta_s$ and $r_t = \Delta_t$.

We implemented the accelerated SF projector in an ANSI C MEX routine using single precision. The DD projector was provided by De Man *et al.*, which is also implemented as a C MEX interface to C code.

1) *Maximum Errors of Forward Projectors:* We define the maximum error as

$$e_k(\beta; \vec{n}) = \max_{s, t \in \mathbb{R}} |F(s, t; \beta; \vec{n}) - F_k(s, t; \beta; \vec{n})|, \quad (9)$$

where $k = 1$ stands for the accelerated SF projector and $k = 2$ stands for the DD projector. We generated the true footprint $F(s, t; \beta; \vec{n})$ in (4) by linearly averaging 1000×1000 analytical line integrals of rays sampled over each detector cell.

We compared the maximum errors of the accelerated forward SF and DD projectors for a voxel with $\Delta_x = \Delta_y = \Delta_z = 1\text{mm}$ centered at the origin. Since the voxel is centered at the origin, we choose $N_\beta = 180$ angles over only 90° rotation. Fig. 2 shows the results on a logarithmic scale. The maximum errors of the DD projector are much bigger than those of the accelerated SF projector, *e.g.*, the maximum error of the DD projector is $0.3/(4.63 \times 10^{-4}) \approx 649$ times of the proposed method when $\beta = 45^\circ$.

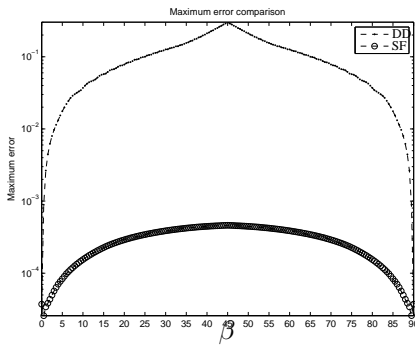


Fig. 2. Maximum error comparison between the accelerated forward SF and DD projector.

2) *Accuracy and Speed of Forward Projectors:* We compared the accuracy and computation times of the accelerated SF and DD forward projectors using an image containing 10 voxels centered at the $z = 0.5\text{mm}$ plane. The size of the image is $N_1 = 512, N_2 = 512, N_3 = 128$ with $\Delta_x = \Delta_y = \Delta_z = 1\text{mm}$ in the x, y, z direction respectively. The transaxial centers of the voxels were chosen randomly. The “gold standard” reference sinogram was generated by linearly

| Forward projectors | SF | DD |
|----------------------------|-----|------|
| max % error | 3.4 | 17.4 |
| % nrms error | 2.3 | 8.1 |
| computation time (seconds) | 158 | 172 |

TABLE I
COMPARISON OF SF AND DD FORWARD PROJECTORS

averaging 8×8 analytical rays sampled across each detector cell. For the two projectors, we computed the normalized maximum error, $\max_i(|x_i - y_i|) / \max_i(|x_i|)$, and normalized root-mean-square (NRMS) error, $\|x_i - y_i\|_2 / \|x_i\|_2$. We evaluated both projectors using 4 threads as computational cores on a computer with Quad-Core Intel Xeon Processor X3230 (8M Cache, 2.66 GHz, 1066 MHz FSB).

Table I summarizes the comparisons of accuracy and computation times. The accelerated SF forward projector is more accurate than the DD forward projector, and the computation time (using Matlab elapsed time commands) is about the same (of course, the execution times depend on code implementation).

B. Forward and Back-projectors within Iterative ROI Reconstruction

In many cases, the region of interest (ROI) is much smaller than the field of view (FOV) that covers the whole irradiated volume. If the ROI were known in advance, the reconstruction could save resources in terms of computation time and memory usage. Ziegler *et al.* [7] proposed the following solution to iterative reconstruction of a ROI.

- 1) Iterative reconstruction of the whole FOV, yielding an initial estimate \hat{x} of x which is the vector representation of the object $f(\vec{x})$.
- 2) Define $\hat{x}_{mask} = \hat{x} \cdot \mathbf{m}$ where $\mathbf{m} = (m_1, \dots, m_p)$ with $0 \leq m_j \leq 1 (j = 1, \dots, p)$ is a mask vector setting the estimated object \hat{x} , inside the ROI to zero and provides a smooth transition from the ROI to the remaining voxels.
- 3) Compute $\mathbf{p}_{out} = \mathbf{A}\hat{x}_{mask}$ which is the forward projection of the masked object \hat{x}_{mask} .
- 4) Obtain the projection of ROI, $\mathbf{p}_{roi} = \mathbf{p} - \mathbf{p}_{out}$ where $\mathbf{p} = \mathbf{A}\mathbf{x}$.
- 5) Iterative reconstruction of the ROI only from \mathbf{p}_{roi} . Due to the transition zone, the region of this reconstruction needs to be extended slightly from the predetermined ROI.

This method requires accurate forward and back projectors. Errors in step 2, where re-projection of the masked estimation image is computed, can greatly affect the results of subsequent iterative ROI reconstruction. Moreover, for iterative image reconstruction, even small approximation errors might accumulate after many iterations. We evaluated the accuracy of our proposed accelerated SF projector and the DD projector in this iterative ROI reconstruction method.

We simulated the GE LightSpeed X-ray CT system with an arc detector of 888 detector channels for 64 slices ($N_s = 888, N_t = 64$) by $N_\beta = 984$ views over 360° . The size of each detector cell is $\Delta_s \times \Delta_t = 1.0239 \times 1.0964\text{mm}^2$. The source

to detector distance is $D_{sd} = 949.075\text{mm}$, and the source to rotation center distance is $D_{s0} = 541\text{mm}$. A quarter detector offset in the s direction is included to reduce aliasing.

We used a modified 3D Shepp-Logan digital phantom \mathbf{x}_{FOV} that only has ellipsoids centered at the $z = 0$ plane to evaluate the projectors. The brain-size field of view (FOV) is $250 \times 250 \times 40\text{mm}^3$, implying $256 \times 256 \times 64$ voxels with a coarse resolution of $0.9766 \times 0.9766 \times 0.6250\text{mm}^3$. We used the analytical method mentioned above to simulate noiseless cone-beam projection measurements from the Shepp-Logan phantom. Noiseless data is used because we want to focus on the accuracy of projectors. First, an entire FOV image $\hat{\mathbf{x}}_{\text{FOV}}$ with the coarse resolution is reconstructed by the FDK method since there is no noise.

The ROI is chosen to center at the rotation center and cover about $48.8 \times 48.8 \times 12.5\text{mm}^3$ ($50 \times 50 \times 20$ voxels with the coarse resolution). The transition zone directly follows the ROI, and covers about $13.7 \times 13.7 \times 5\text{mm}^3$ ($14 \times 14 \times 8$ voxels with the coarse resolution). To construct a masked image $\hat{\mathbf{x}}_{\text{FOV}}^m$ from $\hat{\mathbf{x}}_{\text{FOV}}$, we removed the ROI and smoothly weighted the voxels corresponding to the transition zone by a 3D separable Gaussian function (see Fig. 3).

For reconstruction of the ROI, we implemented iterative image reconstruction with these two projectors. We ran 300 iterations of the conjugate gradient algorithm, initialized with $\hat{\mathbf{x}}_{\text{ROI}}^0$ which is the linearly interpolated image from $\hat{\mathbf{x}}_{\text{FOV}}$, for the following penalized weighted least-squares cost function with a quadratic roughness penalty (QPWLS-CG):

$$\Phi(\mathbf{x}_{\text{ROI}}) = \sum_{i=1}^{N_d} w_i \frac{1}{2} (y_i - [\mathbf{A}\mathbf{x}_{\text{ROI}}]_i)^2 + \beta R(\mathbf{x}_{\text{ROI}}) \quad (10)$$

$$R(\mathbf{x}_{\text{ROI}}) = \sum_k \psi([\mathbf{C}\mathbf{x}_{\text{ROI}}]_k), \quad (11)$$

where y_i is the negative log of the measured cone-beam projection of ROI, w_i s are statistical weighting factors, \mathbf{A} is the system matrix, \mathbf{C} is a differencing matrix and $\psi(t)$ is the potential function. Here $\psi(t) = t^2/2$, a quadratic penalty. For this simulation, we use $w_i = \exp(-[\mathbf{A}\mathbf{x}_{\text{FOV}}]_i)$ and $\beta = 0.25$. Evaluating the PSF using the approximations described in [10] shows that the FWHM is about $1.37 \times 0.96 \times 0.90\text{mm}^3$ for this value of β .

Fig. 3 shows the axial slices of reconstructed images and their errors. We can see that the accelerated SF projector provides lower artifact levels than the DD projector.

IV. CONCLUSION

We have presented a three-dimensional forward and back projector, named the SF projector for X-ray CT. To further improve the computation efficiency, we also proposed an accelerated SF projector. Our results have shown that the accelerated SF projector is more accurate with similar computational speed than the DD projector. To the best of our knowledge, the DD projector is particularly favorable relative to other previously published projectors in terms of the balance between speed and accuracy.

Approximation of the footprint functions as 2D separable functions is the key contribution of our work. Since the

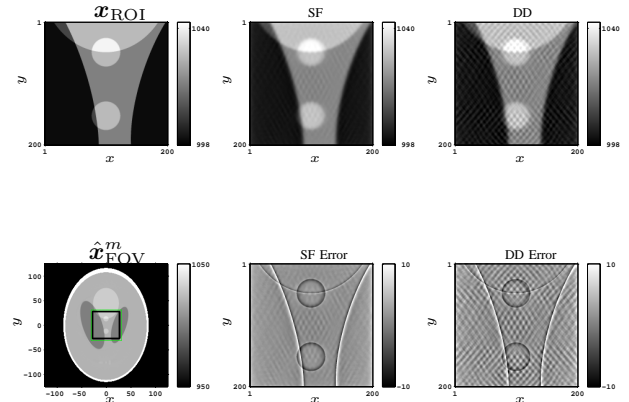


Fig. 3. First column shows the true ROI image and masked estimate image $\hat{\mathbf{x}}_{\text{FOV}}^m$ with the transition zone in black and the region of ROI reconstruction in green lines. Second column shows the reconstructed ROI image and its error from the accelerated SF projector. Third column shows the results from the DD projector. The normalized maximum percent errors are 3.82% and 4.04% for the accelerated SF and DD projector respectively. The NRMS percent errors are 0.91% and 0.92% respectively.

separability greatly simplifies the calculation of integrals of the footprint functions, using more accurate functions in the transaxial direction is possible without complicating significantly the calculation.

ACKNOWLEDGMENT

We thank GE for the use of their DD projector/backprojector code.

REFERENCES

- [1] R. L. Siddon, "Fast calculation of the exact radiological path for a three-dimensional CT array," *Med. Phys.*, vol. 12, no. 2, pp. 252–5, Mar. 1985.
- [2] B. De Man and S. Basu, "Distance-driven projection and backprojection in three dimensions," *Phys. Med. Biol.*, vol. 49, no. 11, pp. 2463–75, Jun. 2004.
- [3] A. Ziegler, T. Köhler, T. Nielsen, and R. Proksa, "Efficient projection and backprojection scheme for spherically symmetric basis functions in divergent beam geometry," *Med. Phys.*, vol. 33, no. 12, pp. 4653–63, Dec. 2006.
- [4] S. Matej and R. M. Lewitt, "Practical considerations for 3-D image reconstruction using spherically symmetric volume elements," *IEEE Trans. Med. Imag.*, vol. 15, no. 1, pp. 68–78, Feb. 1996.
- [5] C. Riddell and Y. Troussset, "Rectification for cone-beam projection and backprojection," *IEEE Trans. Med. Imag.*, vol. 25, no. 7, pp. 950–62, Jul. 2006.
- [6] C. Schretter, "A fast tube of response ray-tracer," *Med. Phys.*, vol. 33, no. 12, pp. 4744–8, Dec. 2006.
- [7] A. Ziegler, T. Nielsen, and M. Grass, "Iterative reconstruction of a region of interest for transmission tomography," *Med. Phys.*, vol. 35, no. 4, pp. 1317–1327, Apr. 2008.
- [8] A. C. Kak and M. Slaney, *Principles of computerized tomographic imaging*. New York: IEEE Press, 1988.
- [9] P. M. Joseph, "An improved algorithm for reprojecting rays through pixel images," *IEEE Trans. Med. Imag.*, vol. 1, no. 3, pp. 192–6, Nov. 1982.
- [10] J. A. Fessler and W. L. Rogers, "Spatial resolution properties of penalized-likelihood image reconstruction methods: Space-invariant tomographs," *IEEE Trans. Im. Proc.*, vol. 5, no. 9, pp. 1346–58, Sep. 1996.